Received: 8 November 2024 | Accepted: 1 April 2025

DOI: 10.1111/mice.13487

RESEARCH ARTICLE

COMPUTER-AIDED CIVIL AND INFRASTRUCTURE ENGINEERING WILEY

# Three-dimensional morphological analysis of Chang'e-5 lunar soil using deep learning-automated segmentation on computed tomography scans

Siqi Zhou[1] | Yu Jiang[2] | Xinyang Tao[1] | Feng Li[1] | Chi Zhang[2] | Wei Yang[2] | Yangming Gao[3]

[1]School of Transportation Science and Engineering, Beihang University, Beijing, China

[2]Key Laboratory of Earth and Planetary Physics, Institute of Geology and Geophysics, Chinese Academy of Sciences, Beijing, China

[3]Highway Engineering Built Environment and Sustainable Technologies (BEST) Research Institute, Liverpool John Moores University, Liverpool, UK

**Correspondence**

Feng Li, School of Transportation Science and Engineering, Beihang University, Beijing, China.
Email: lifeng98@buaa.edu.cn

Chi Zhang, Key Laboratory of Earth and Planetary Physics, Institute of Geology and Geophysics, Chinese Academy of Sciences, Beijing, China.
Email: czhang@mail.iggcas.ac.cn

**Funding information**

National Natural Science Foundation of China, Grant/Award Number: 52308427; Fundamental Research Funds for the Central Universities; China Postdoctoral Science Foundation, Grant/Award Number: 2024T171118; B-type Strategic Priority Program of the Chinese Academy of Sciences, Grant/Award Number: XDB41000000

**Abstract**

Grain morphology is a fundamental characteristic of lunar soil that influences its mechanical properties, sintering behavior, and in situ resource utilization. However, traditional two-dimensional imaging methods are time-consuming and lack full three-dimensional (3D) structural information. This study presents an automated deep learning-based segmentation and reconstruction algorithm for high-resolution X-ray computed tomography scans of Chang'e-5 lunar soil samples. By integrating a U-Net convolutional neural network with a watershed algorithm, this method enables efficient and accurate 3D reconstruction of 553,578 lunar soil particles, significantly reducing manual annotation time. The results reveal a median particle size of 63.73 μm, an average aspect ratio of 0.55, and an average sphericity of 0.87, providing key insights into lunar regolith morphology. A clustering analysis identified 30 representative particle types, whose STereoLithography models will be made publicly available for further research and numerical simulations. These findings offer crucial data for discrete element modeling, thermal analysis, and engineering applications, supporting future lunar exploration and the development of sustainable lunar infrastructure.

## 1 | INTRODUCTION

With the resurgence of global interest in lunar exploration (Li et al., 2019; Mandt, 2024; Schörghofer & Rufu, 2023), the focus has shifted to crewed lunar landings, lunar exploration activities, and lunar base construction (Bao et al., 2024; Y. Wang et al., 2022). The effective execution of these plans depends on attaining various essential engineering goals, including the secure landing and launching of spacecraft, as well as the development and guidance of lunar rovers (Chien et al., 2024; Ding et al., 2024), and the utilization of in situ lunar resources (Yao et al., 2022; S. Zhou et al., 2021).

Understanding the three-dimensional (3D) morphological properties of lunar soil particles provides critical scientific data necessary for tackling these major engineering challenges. For instance, the interaction between lunar soil and rocket exhaust plumes during lander takeoff and landing can alter the gas-solid coupling flow process under plume impact (Metzger et al., 2011; Sarwar & Hasnain, 2024), leading to the phenomenon of lunar dust lofting, which obstructs visibility. The resulting erosion pits can damage the lunar surface, posing safety hazards. This process is significantly influenced by the size and surface morphology of the lunar soil. Additionally, the mechanical as well as flow properties are mainly affected by the shape, size, and surface roughness (L. Yang et al., 2020). Examining these properties sheds light on the mechanisms governing the mechanical behavior of lunar soil, clarifies its interaction with rover wheels (Ding et al., 2022) to prevent immobilization, and supports the excavation and sampling processes. Additionally, understanding the 3D morphological characteristics of lunar soil particles is essential for lunar infrastructure development, including the construction of landing pads, roads, and 3D-printed regolith structures (R. Zhang et al., 2022; C. Zhou et al., 2024). The mechanical behavior of lunar soil, particularly its compaction, load-bearing capacity, and interlocking effects, is directly influenced by particle shape and roughness. These properties also play a crucial role in sintering and geopolymer-based hardening techniques, where irregular particle shapes create voids that hinder heat transfer, potentially leading to defects in fabricated materials (Gupta et al., 2024). The detailed 3D reconstruction and classification of lunar regolith particles in this study provide critical input for discrete element method (DEM) simulations, which are widely used in civil engineering to model granular mechanics and predict material behavior under different loading conditions.

Grain morphology information, represented by particle size distribution, is one of the fundamental geological and geotechnical classification parameters of lunar regolith. It reflects the degree of space weathering caused by meteorite impacts and contains information on the evolution of lunar soil. The particle shape of lunar regolith also influences its mechanical strength, compressibility, thermal, optical, and seismic properties. The National Aeronautics and Space Administration has conducted detailed morphological analysis on 143 samples collected from the Apollo and Luna missions (Graf, 1993). The Chang'e-5 lunar regolith was collected from the northeastern edge of Oceanus Procellarum, a location distinct from previous lunar sample sites, providing an opportunity to enhance the comprehensiveness of lunar morphology studies (Y. Chen et al., 2023).

However, the limited quantity and precious nature of these samples necessitate non-destructive methods to study them. Current research methods have limitations. Traditional particle size analysis methods include electrical resistance, sedimentation, microscopy, light scattering, and sieving. Existing studies on lunar soils mainly rely on scanning electron microscopy (SEM) or optical microscopy (Cao et al., 2022; Li et al., 2022; H. Zhang et al., 2021), which can only capture two-dimensional (2D) projections of the particles and lack 3D morphological and surface texture information. Moreover, these methods often damage the valuable lunar soil samples. SEM requires coating the non-conductive lunar soil with gold, while light scattering, sedimentation, and electrical resistance methods require ultrasonic dispersion of the soil in water or other solvents, contaminating the samples and making them unrecoverable. Sieve analysis is usually only suitable for particles with a particle size larger than 10 μm. However, lunar soil particles have poor sorting properties, with a considerable proportion of tiny particles under 10 μm (Carrier et al., 1991). Additionally, the extremely low conductivity of lunar soil causes electrostatic attraction, leading particles to cling to the sieve and complicating sample recovery (Olhoeft et al., 1974). These methods usually require selecting dozens to hundreds of particles from lunar soil samples for observation, which is time-consuming, labor-intensive, and risks damaging the samples, disrupting the spatial structure and altering particle positions.

3D X-ray computed tomography (CT) technology presents a new way for non-destructive testing of the 3D morphology of lunar soil (D. Chen et al., 2024). The process of 3D reconstruction using CT images primarily involves several steps: acquisition of 2D tomographic images, image segmentation, 3D reconstruction, model measurement and statistical analysis, and result validation.

Accurate segmentation algorithm of lunar soil particles and the voids created by their accumulation is crucial for measuring the 3D morphology of lunar soil using CT images. Traditional segmentation methods include intensity thresholding, area expansion, and boundary detection, all of which focus on using grayscale thresholds to differentiate target particles from background voids. However, since individual lunar soil particles may contain various minerals, presenting different grayscale values in CT slice images, these grayscale-based methods tend to divide a multi-mineral particle into several segments. Additionally, for high-resolution CT images of fine lunar soil particles, the manual correction process based on grayscale thresholds can be time-consuming and labor-intensive.

The use of deep learning algorithm, particularly the U-Net architecture, for segmenting CT images has been widely applied in fields such as medical imaging (J. Wang et al., 2023), biology (Falk et al., 2019; Rafiei et al., 2022), image classification (Alam et al., 2020), marine sedimentology (Mitra, et al., 2024), battery design (Lu et al., 2020), vehicle detection (García-Aguilar et al., 2023), concrete strength estimation (Rafiei et al., 2017), and numerical computation acceleration (Pereira et al., 2020) effectively addressing variability and complexity in data (De Nardin et al., 2023; Sun et al., 2024). However, its application in the segmentation of lunar soil particles remains limited. The data-driven learning process holds promise for resolving the issue of varying grayscale voxels within single lunar soil particles.

To address these issues, this research utilizes actual lunar soil particles from the Chang'e-5 mission and employs high-resolution X-ray CT images technology to scan the images of lunar soil samples. Deep learning techniques are used to automatically process the slice data for particle identification and segmentation, enabling 3D reconstruction. This approach has established a vast digital model library of lunar soil particles and measured 3D morphological parameter of the lunar sample.

This method offers several advantages. First, it is nondestructive (Katagiri et al., 2015), as the lunar soil is only exposed to X-ray irradiation without any additional damage or loss in quantity. Second, it captures the 3D characteristics and spatial packing structures of the particles (Lu et al., 2020). Third, the process is automated, which significantly saves time and effort (Falk et al., 2019). The comprehensive and precise 3D morphological data of lunar soil provided by this study serve as fundamental data for discrete element modeling and thermal analysis of lunar soil particles in engineering research. This research provides key insights into the mechanical properties and behavior of lunar soil, aiding the progress of lunar exploration initiatives and the development of sustainable lunar bases.

## 2 | PARTICLE SEGMENTATION AND 3D RECONSTRUCTION OF CT-SCANNED IMAGES FROM LUNAR SAMPLE

### 2.1 | Preparation of the Chang'e-5 lunar samples

On December 17, 2020, the CE-5 lunar samples were returned to Earth and stored at the National Astronomical Observatories, Chinese Academy of Sciences, with a total weight of approximately 1731 g. The samples were categorized into scooped (CE5C) and drilled (CE5Z) types, based on two sampling methods. The scooped samples, collected from four points at a depth of ∼3 cm, were transferred into a 16 cm square stainless-steel container, mixed thoroughly, and rock fragments larger than 1 mm were removed. A 12 g portion was randomly scooped from 10 of the 16 divided squares and placed into separate bottles (CE5C0100–CE5C1000). This process was repeated 13 times to ensure sample homogeneity. All handling occurred within a sealed, nitrogen-filled glove box, with water and oxygen levels kept below 1 ppm to prevent contamination and preserve sample integrity (Li et al., 2022).

### 2.2 | X-ray CT

Approximately 30 mg of regolith from the CE5C0400YJFM00406 subsample, originally taken from the CE5C0400 bottle, was transferred into a quartz tube with an inner diameter of 2 mm. The sample was then scanned with high-resolution X-ray CT of FEI Heliscan MicroCT. During the process, the sample stage rotated and moved along a helical path, capturing thousands of projections at an isotropic voxel size of 0.9923 μm and a field of view of 2861 × 2861 μm. The source voltage is 80 kV, and the source current is ∼90 μA. One thousand slice radiographs in the center part were selected for image processing. A cylindrical shape tool was used to select the lunar soil sample area as the region of interest for analysis.

The Chang'e-5 sample consists of soil particles and voids between the particle-overlapping skeleton. Figure 1 shows a typical CT scan slice image. The prerequisite for reconstructing particles from CT images is the precise segmentation of lunar soil particles and voids in 2D slices. The gray value is proportional to the X-ray attenuation coefficient of the substance, based on which the particle segmentation is performed. Unlike CT images of homogeneous materials where the interior of particles typically exhibits uniform grayscale values (Lu et al., 2020), lunar soil is a mixed-phase material composed of plagioclase,

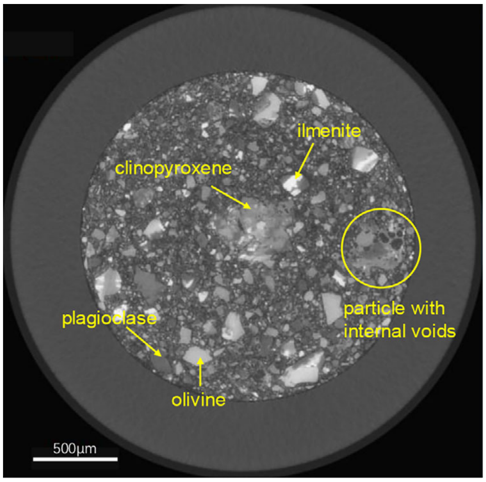


**FIGURE 1** A typical computed tomography (CT) scan slice of Chang'e-5 lunar soil sample.

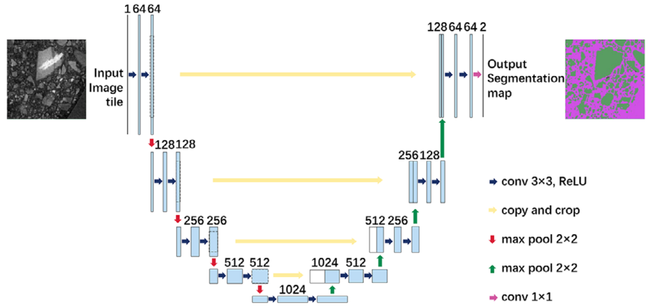


**FIGURE 2** U-Net architecture used for the initial segmentation of lunar soil particles and pores. ReLU, rectified linear unit.

clinopyroxene, ilmenite, olivine, and other trace minerals (Hu et al., 2021; Y. Jiang et al., 2022). Different minerals have varying X-ray absorption rates, resulting in different grayscale regions within a single particle. This variability complicates traditional segmentation methods that rely on grayscale thresholding, as different grayscale regions within the same particle may be identified as separate particles. Additionally, it is worth noting that some lunar soil particles contain internal voids, which can cause interruptions in particle images in 2D slices, further complicating segmentation.

### 2.3 | Image binarization and particle segmentation using U-Net deep learning network and watershed algorithm

The purpose of the binarization is to separate the lunar soil particle and pores in the X-ray radiographs of lunar samples. In this study, a U-Net architecture (Ronneberger et al., 2015) was utilized for image segmentation. The prepared dataset consists of horizontal scan sections of CT data, where both lunar soil particles and voids were labeled. U-Net is a convolutional neural network originally developed for biomedical image segmentation (Ronneberger et al., 2015). It consists of an encoder–decoder architecture, where the encoder extracts hierarchical spatial features, while the decoder reconstructs the segmentation mask. The segmentation output ($x_{,,}$) can be represented as Equation (1):

$$S(x, y, z) = \sigma\left(W_d \cdot \mathrm{ReLU}\left(W_e \cdot I(x, y, z) + b_e\right) + b_d\right) \tag{1}$$

where $I(x, y, z)$ represents the input 3D CT image; $W_e, b_e$ are the encoder weights and biases, respectively; $W_d, b_d$ are the encoder weights and biases, respectively; and $\sigma$ is the softmax activation function. The ReLU (i.e., rectified linear unit) function introduces non-linearity, ensuring effective feature extraction by setting negative values to zero while preserving positive activations.

During the segmentation process, particles were marked as positive samples, while voids were treated as negative (background) regions. Manual annotation was performed on a subset of the CT slices to generate ground truth labels, ensuring accurate particle and void segmentation. This approach allowed the model to differentiate between particles with varying grayscale values and internal voids, enhancing segmentation accuracy in mixed-phase materials. The network architecture is shown in Figure 2. The model was implemented using Python 3.11 and Pytorch 2.1.0. All experiments were conducted on a system equipped with an Intel Xeon w7-2475X CPU and two NVIDIA GeForce RTX4090 GPUs. The experimental dataset comprised 100 manually annotated radiographs of lunar soil particles and pores. The images were randomly divided into a training set and a validation set in an 8:2 ratio. During model training, the following hyperparameters were configured: the input (patch) size was set to 64, the stride-to-input ratio was 0.5, the number of epochs was 100, and the batch size was 32. The loss function used was categorical cross-entropy, and the optimization algorithm employed was Adam, resulting in the determination of the optimal hyperparameters for the model.

The next step in the process is particle segmentation, which involves further extracting individual particles from the binarized results. Traditional segmentation methods (e.g., Otsu thresholding, region-growing algorithms) struggle with lunar soil CT images due to overlapping grayscale values of different minerals and the presence of internal voids (Yu et al., 2025). Therefore, we integrate U-Net with a watershed algorithm (Vincent & Soille, 1991) to refine boundaries. The process included steps of grayscale conversion, noise reduction, thresholding, distance transform, marker identification, and watershed transformation. Finally, segmented particle images from various slices were combined to reconstruct the 3D structure of lunar soil particles.

## 3 | 3D MORPHOLOGY OF LUNAR SOIL PARTICLES

This article comprehensively characterized the 3D morphology of lunar soil particles, primarily analyzing the particle size and spatial distribution, shape, and surface roughness.

### 3.1 | Spatial position distribution and size distribution

The geometric center of each particle was determined by calculating the arithmetic mean of the coordinates of the centers of all voxels within the particle. Ignoring the uneven density distribution caused by different mineral compositions of lunar soil particles, this geometric center also served as the particle's centroid.

In terms of size characterization, the voxel count, volume, equivalent spherical diameter (ESD), and average Feret diameter were used. The volume of a single lunar soil particle was calculated by multiplying the number of voxels comprising the lunar soil particle (voxel count) by $0.9923^3$ $\mu m^3$. The equivalent sphere diameter refers to the diameter of a sphere with the same volume as the lunar soil particle, while the average Feret diameter is the mean of the longest linear dimensions of particle projections measured in different directions. A spherical coordinate system was established at the centroid, and the steps for azimuth angle ($\Phi$) and polar angle ($\theta$) were set to 10 degrees, covering all angle combinations to span 360 degrees of azimuth and 180 degrees of elevation. The Feret diameter was measured for each angle combination to obtain the average Feret diameter.

### 3.2 | Shape analysis

In shape analysis, the aspect ratio and sphericity were used for description. The aspect ratio is the ratio of the smallest to the largest side length of the particle's minimum bounding box (Michikami et al., 2018). The aspect ratio values span from 0 to 1, where values nearer to 0 represent more elongated particles, while values closer to 1 signify particles approaching the shape of a perfect cube or sphere. Sphericity was measured by calculating the ratio of the object's volume to its surface area as defined in Equation (2) (Graf, 1993), where $S$ is sphericity, $V_\mathrm{p}$ is volume of the particle, and $S_\mathrm{p}$ is the surface area of the particle. In terms of the overall characteristics of surface roughness, the total roughness proxy (TRP) was used for quantification, which reflected the difference between the smallest and largest radii observed across all three planes, thus providing a quantitative indicator of the object's surface irregularity.

$$S = \sqrt[3]{36\pi V_\mathrm{p}^2}/S_\mathrm{p} \tag{2}$$

### 3.3 | Clustering analysis and local roughness

Using the K-means algorithm (Ikotun et al., 2023), a clustering analysis was performed on the mean Feret diameter, aspect ratio, sphericity, surface area, ESD, TRP of all segmented Chang'e-5 lunar soil particles, with total number of clusters set to 30, followed by local roughness calculations for representative particles using marching cubes to create STereoLithography (STL) files, spherical harmonic fitting for a smooth reference surface, and visualizing roughness distribution and shape.

## 4 | RESULTS OF SEGMENTATION AND 3D RECONSTRUCTION

### 4.1 | Training results of binarization based on U-Net model

The model training outcomes are assessed through two metrics: the cross-entropy loss function and the Dice evaluation coefficient. A lower loss function value and a Dice coefficient nearing 1 suggest improved model performance. Figure 3 illustrates the variation in loss function values and the Dice coefficient as training iterations increase.

In the training of a U-Net model for binarization of lunar soil particles from 3D X-ray radiographs data, the observed loss metrics indicated a promising learning progression (Figure 3a). As shown in the training curve, both the training and validation losses dropped significantly in the early epochs, indicating that the model quickly learned the relevant features. Post approximately 20 epochs, the rate of decline plateaued, signaling the onset of convergence. Notably, the training loss consistently maintained a lower value, compared to the validation loss, indicating no significant overfitting and affirming the model's ability to generalize. The validation loss, after reaching a nadir, remained relatively stable, a desirable outcome that underscores the model's robustness against overfitting. The low magnitudes of both losses at convergence imply a

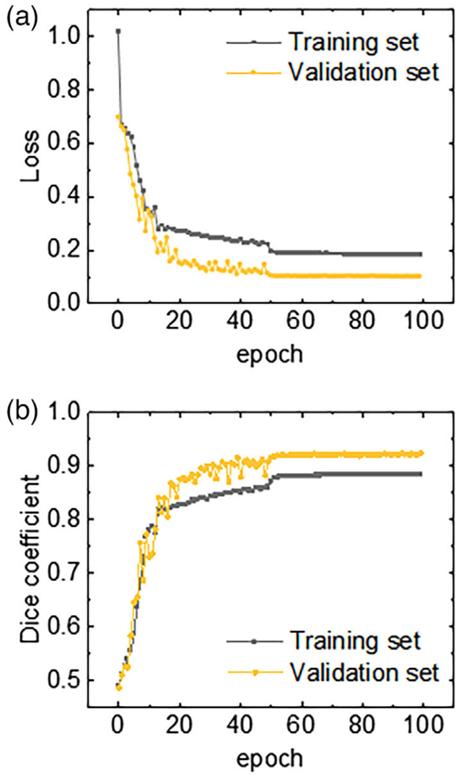


**FIGURE 3** Training and validation (a) loss curves and (b) Dice coefficient curves for U-Net based segmentation of lunar soil three-dimensional (3D) X-ray microscope.

satisfactory performance in binarization the lunar soil particle 3D X-ray microscope data, warranting the potential applicability of the model in practical scenarios. Further model refinement could be pursued by fine-tuning hyperparameters or extending data augmentation strategies, should the necessity for improved validation performance be identified.

Moreover, as shown in Figure 3b, the Dice coefficient for both the training and validation sets increased rapidly in the initial stages and stabilized after approximately 20 epochs. The validation set achieved a slightly higher Dice coefficient than the training set, indicating the model's strong generalization capability. At convergence, the segmentation model achieved a Dice coefficient of 0.91, demonstrating its effectiveness in accurately binarizing lunar soil particles for automatic segmentation of X-ray radiographs. This corresponds to an approximate 9% area discrepancy, compared to the ground truth, which is acceptable for large-scale morphological analysis. However, minor uncertainties may arise in extracted parameters such as aspect ratio, sphericity, and roughness, particularly for small particles where boundary inaccuracies have a greater proportional impact. Nonetheless, given the dataset size (553,578 particles), such variations do not significantly affect the overall statistical trends.

### 4.2 | Particle identification and segmentation results

Figure 4a shows a typical CT scan slice and an image of a cylindrical lunar soil powder sample composed of 1000 slices. The segmentation results are shown in Figure 4b. Lunar soil particle regions are represented in green and void regions in magenta. A corner of the 3D model is cut away to show the internal structure of the segmented image. The results show that the model effectively segmented lunar soil particles and voids in the slice images, completing the process in just 17 h, 17 min, and 15 s, greatly reducing the time, compared to manual annotation. As seen in Figure 5, the segment method based on U-Net proposed in this study can accurately identify lunar soil particles with internal voids and those containing more than two types of minerals. Additionally, the voxel volume of lunar soil particles is 1,365,512,332 μm$^3$, and the void volume is 1,635,560,668 μm$^3$. By taking the ratio of these two volumes, the void ratio is calculated to be 1.20. The reported values for the void ratio of lunar soil samples range between 0.67 and 2.37 (McKay et al., 1974). The results from CT image processing fall within this range, also proving the effectiveness of the segmentation algorithm.

Figure 4c,d shows the results of using the watershed algorithm to identify particles in the segmented images, with a total of 773,539 lunar soil particles segmented. A cylindrical shell matching the size of the original slice data's 3D reconstruction was constructed, and Boolean operations were used to subtract particles intersecting with the cylindrical shell. The shape information of these boundary particles was not completely scanned, so they needed to be removed. Finally, a total of 724,470 complete lunar soil particles were obtained as shown in Figure 4e. It can be seen that many voids appear in the outer shell region of the 3D model, which are the locations where particles have been removed.

## 5 | 3D MORPHOLOGICAL CHARACTERISTICS

### 5.1 | The size and spatial distribution of lunar soil

The lunar soil particles with sizes similar to the scanning resolution are difficult to distinguish in the Micro-CT scanned images, which can lead to misjudgments during image annotation and U-Net network recognition. This study assumes that particles with volumes smaller than 27 voxels are misjudgments caused by instrument error or noise. After removing these particles, a total of 553,578

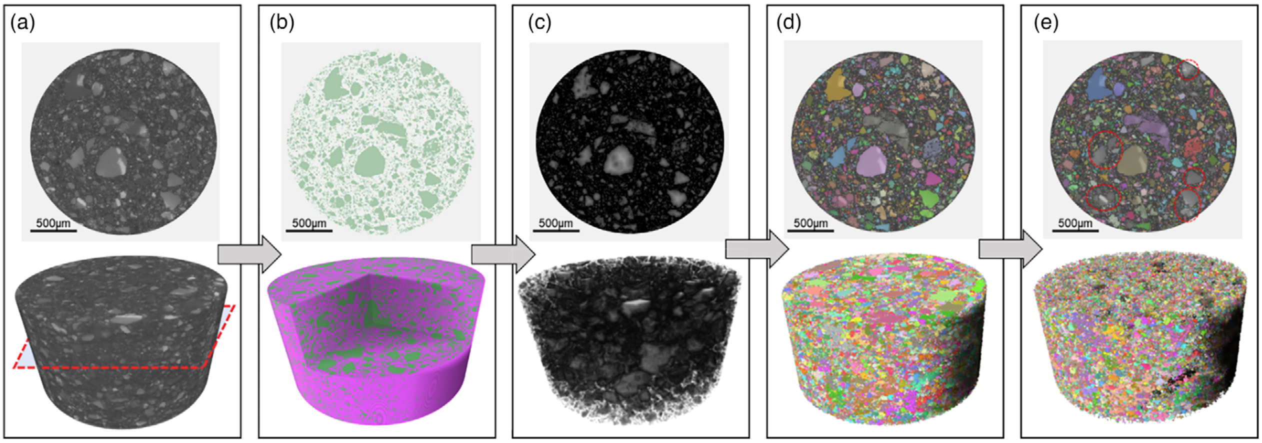


FIGURE 4 Chang'e-5 lunar sample 3D reconstruction and particle segmentation workflow based on U-Net deep learning network and watershed algorithm. (a) The raw data of reconstructed grayscale images with a spatial resolution of $0.9923 \times 0.9923 \times 0.9923\ \mu m^3$. The cross-section marked with a red dotted box shows the position of the displayed slice in the model. (b) Utilizing the U-Net for the segmentation of two-dimensional (2D) slices, the image types are divided into two categories: particles and pores. The segmentation results are reconstructed in three dimensions, with green representing particles and magenta representing pores. (c) The identification of local minima in the resulting images from U-Net segmentation and the construction of the gradient magnitude map based on these minima. (d) The application of the watershed algorithm on the gradient magnitude map to determine the boundaries between particles and pores, enabling the individual classification of each particle. (e) A reconstruction model of lunar soil particles containing 724,470 particles was obtained after particles that intersect the scanning boundary are removed. In the 2D slices, the region of interest was deleted, as indicated by the red dashed line circle marking the removed particles.

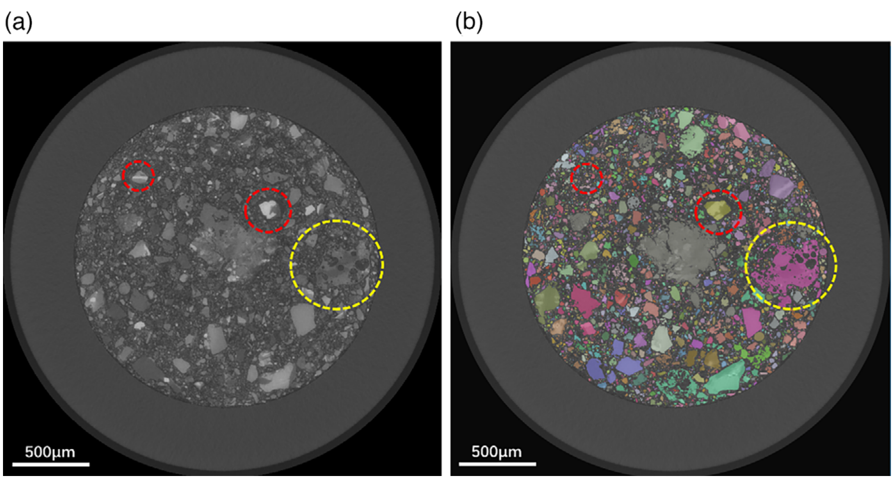


FIGURE 5 A representative slice from the 3D X-ray microscope scan. (a) Original scan and (b) particle identification results, accurately segmenting particles with internal pores (yellow circles) and multi-mineral compositions (red circles) despite grayscale variations.

particles were obtained for statistical analysis of the 3D morphological parameters of the lunar soil. The 27-voxel threshold was selected based on the resolution of the CT scans (0.9923 μm per voxel), corresponding to an ESD of approximately 3.69 μm. Objects below this size are likely to represent noise or segmentation artifacts rather than true lunar soil particles. Removing these particles minimized noise interference and enhanced the accuracy of the particle size distribution analysis. The frequency distribution histograms of ESD and the average Feret diameter are shown in Figure 6a,b. The ESD ranges from 3.69 to 507.64 μm, with mean, median, and mode values of 7.84, 6.00, and 7.67 μm, respectively. The average Feret diameter ranges from 4.00 to 865.28 μm, with mean, median, and mode values of 9.91, 7.36, and 7.47 μm, respectively. The size of the equivalent diameter is related only to the particle volume, while the average Feret diameter is influenced by the different contour sizes of irregular lunar soil particles

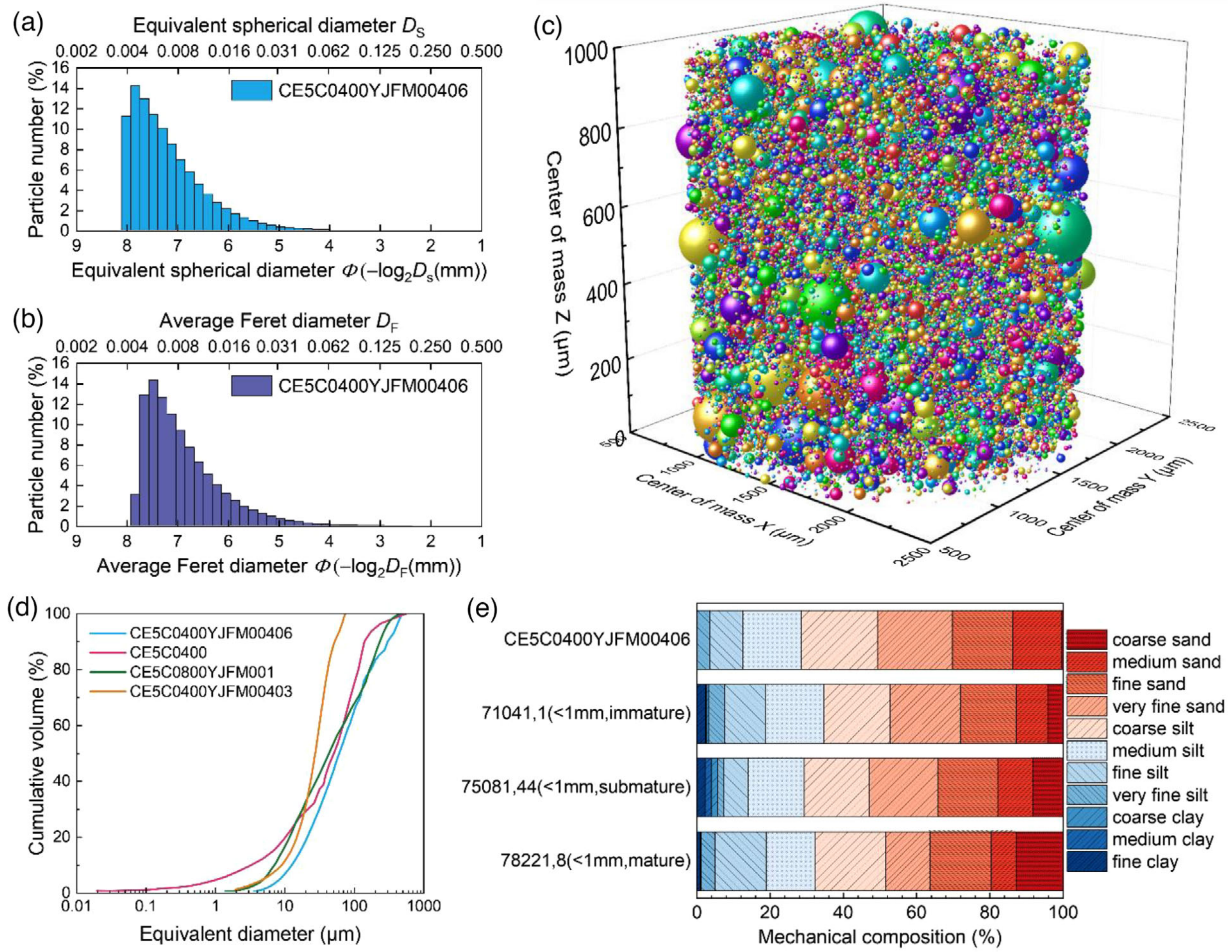


**FIGURE 6** Particle size measurement and 3D spatial distribution of Chang'e-5 lunar soil particles. The frequency distribution histogram displays (a) equivalent spherical diameter (ESD) and (b) average Feret diameter. Lower horizontal axis represents particle size as $\Phi$, where $\Phi = \log_2 D_i$. $D_S$ and $D_F$ ESD and average Feret diameter, respectively, measured in millimeters. The upper horizontal axis displays particle sizes in millimeters. (c) 3D centroid positions of particles, with sphere sizes representing $D_F$ (some omitted for clarity). (d) Cumulative volume distribution of equivalent diameters from different methods: Micro-CT (this study, blue), laser particle size analysis (H. Zhang et al., 2021, rose), optical microscopy (Li et al., 2022, green; Zhang et al., orange). (e) Volume-based mechanical composition comparison between Chang'e-5 and Apollo 17 lunar soils of varying maturity (McKay et al., 1974).

projected in different directions. Therefore, the statistical values of the two parameters differ.

The centroid coordinates of 553,578 particles are calculated and visualized using spheres of varying diameters to represent the average Feret diameters as illustrated in Figure 6c. To ensure clarity in the display, some particles are omitted from the figure. However, the centroid coordinates and average Feret diameters of all 553,578 particles are available on request from the authors for future numerical modeling. The precise arrangement of the lunar soil particles, with accurate coordinates and size data, allows for exact geometric modeling of the lunar soil matrix in DEM simulations (M. Jiang et al., 2013; S. Wang & Jiang, 2024). This enhances the model's realism and relevance in reflecting the soil's behavior under various physical conditions. DEM simulations require a realistic representation of the material to accurately predict its behavior under different loading conditions. The initial spatial arrangement of the particles influences their interactions during the simulation. Capturing this arrangement accurately ensures that the simulation closely mirrors the true behavior of lunar regolith. The initial spatial distribution affects the number and distribution of contacts between particles, which in turn influences the overall mechanical response, such as stress distribution, strain, or failure patterns. The data offer a scientific basis for precise modeling in discrete element simulations, ensuring that the simulation parameters reflect the actual conditions experienced by lunar regolith.

The cumulative volume distribution of the ESD of CE5C0400YJFM00406 is shown in Figure 6d. Particle size distribution parameters can be derived by selecting specific percentile sizes from the cumulative frequency diagram on a log-probability graph. The definition of a percentile ($d_n$) means that at the $n$th percentile, $n$% of the sample has a particle size less than this value, leading to effective grain size $d_{10}$, middle grain size $d_{30}$, median grain size $d_{50}$, and constrained grain size $d_{60}$, which are 13.45, 33.10, 63.73, and 89.28 μm, respectively. This indicates that most particle sizes are concentrated around 60 μm. A small $d_{50}$ value suggests a high degree of maturity for the lunar soil sample, reflecting its monodisperse nature. Recent reports have also confirmed the maturity of this lunar soil (Li et al., 2022; H. Zhang et al., 2021). Further calculation obtained coefficients of uniformity $C_u$ and curvature $C_c$ of 6.63 and 0.91, respectively, indicating A $C_u$ greater than 5 indicates that there are sufficient finer particles in the lunar soil to fill the voids between the coarser particles, resulting in a denser soil structure. However, the relatively small $C_c$ suggests a step within the range from $d_{30}$ to $d_{60}$, indicating a lack of certain particle sizes within this range. The mean, skewness, and kurtosis are 101.87 μm, 0.64, and 1.36, respectively. A positive skewness suggests that the particle distribution tends toward finer particles. The kurtosis value, being less than 3, shows that the particle distribution is flatter than a normal distribution.

The cumulative volume distribution of particle sizes of lunar soil tested by the other three different laboratories is shown in Figure 6d. The four curves are close but not identical. $D_{50}$ of CE5C0400 (H. Zhang et al., 2021), CE5C0800YJFM001 (Li et al., 2022), CE5C0400YJFM00403 (Cao et al., 2022) is 55.24, 52.54, 28.72 μm, respectively. The most significant variations occur at the smallest particle sizes. The difference should be related to not only the distinction caused by Chang'e-5 samples in different batches but the measurement method. The particle size of sample CE5C0400 was measured using a laser granulometer, which has a measurement range of 0.1 to 3500 μm. This explains why CE5C0400 includes measurements in the smaller particle size range. Samples CE5C0800YJFM001 and CE5C0400YJFM00403 were analyzed by dispersing the lunar soil in a solution, then dropping it onto aluminum-coated glass slides and counting the particles by an optical microscope with a resolution of 0.4 μm. The particle size distribution results indicate that CE5C0400YJFM00403 has finer measurements, compared to CE5C0800YJFM001. The overestimation of smaller particle sizes could result from overexposure in the dark-field imaging needed to detect them.

The results of the four size measurements are grouped by coarseness according to the clastic sediment classification method (Udden, 1914; Wentworth, 1922) as shown in Figure 6e. These groups are referred to as grades. Each grade includes particles within a size range defined by two adjacent separations. The diameter of fine clay ranges from 1/2048 to 1/1024 μm. Gravel refers to particles larger than 1 mm. These separations follow a uniformly decreasing series of diametrical dimensions, ensuring that the largest particles in each grade have twice the diameter of the largest particles in the next finer grade, from the coarsest to the finest. In the Chang'e-5 lunar soil sample used in this study, coarse silt with the particle size ranging from 31.25-62.50 μm is present in greater quantity (20.85%) than any other, which is called the major grade. The content proportions of very fine sand (62.5–125 μm) and medium silt (15.63–31.25 μm) are 20.46% and 15.91%, ranking second and third, respectively, and are referred to as the secondary major grades.

In the process of lunar surface weathering (Liu et al., 2024; Wu et al., 2023; Zeng et al., 2024), as the exposure time on the lunar surface increases, the lunar soil develops from immature to submature and finally to mature. This process gradually decreases coarse particles while increasing fine ones. The particle classification results of representative lunar soil samples collected by Apollo 17 at various stages of maturity (McKay et al., 1974) are shown in Figure 6e. Due to the removal of particles larger than 1 mm during the Chang'e-5 lunar soil sampling process, particles smaller than 1 mm in the Apollo sample were selected for grading comparison. As the lunar soil matures, the content of the larger particles, specifically the coarse sand grades, significantly decreases. It can also be observed that the major grade and the secondary major grades of the Chang'e-5 sample fall between the mature (78221,8) and submature (75081,44) samples, but they lack large particles in the coarse sand grade. Therefore, the lunar soil is more inclined to be classified as mature lunar soil, aligning with the findings of Li et al. (2022). It is important to note that although classification criteria based on terrestrial sedimentology have been adopted as a reference framework to facilitate comparison with existing research, the significant differences between lunar soil and terrestrial soils in terms of genesis, mineral composition, and physical properties are fully recognized. Therefore, this classification method is employed solely as a descriptive tool with inherent limitations, and future research will aim to develop particle classification standards that are better suited to the unique characteristics of lunar soil.

### 5.2 | 3D shape characteristics of lunar soil characterized by aspect ratio and sphericity parameters

The aspect ratio results show that lunar soil is slightly to moderately elongated. The aspect ratio is an indicator of the elongation of particles. The closer the aspect ratio is to 0, the more elongated the particle; the closer it is to 1,

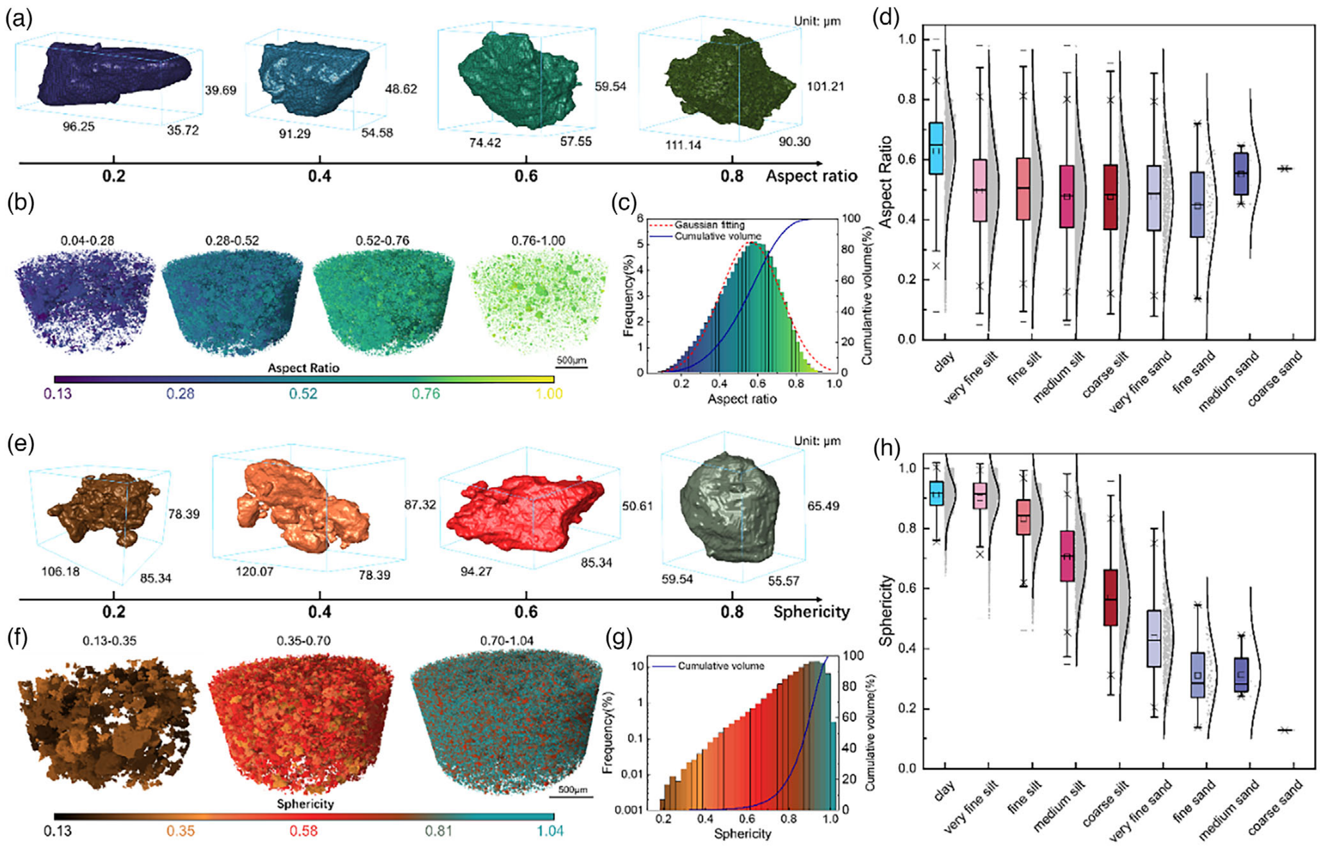


**FIGURE 7** Three-dimensional shape parameters of Chang'e-5 lunar soil samples. (a, e) Selected 3D models of particles with varying aspect ratios (0.2–0.8) and sphericity values (0.2–0.8); (b, f) particle distributions based on aspect ratio and sphericity, with colors representing different values; (c) histogram of aspect ratio distribution for 553,578 particles, with Gaussian fitting ($R^2 = 0.98$, mean = 0.56); (d) box plot of aspect ratio across different size classes; (g) histogram of sphericity distribution; (h) box plot of sphericity across different size classes.

the more it approaches an ideal sphere or cube as shown in Figure 7a. Figure 7b displays the distribution of particles in the original 3D model, categorized by aspect ratio, showing the spatial distribution of these ratios within the sample. Figure 7c presents a frequency histogram detailing the aspect ratio frequency distribution of 553,578 particles, indicating common and rare particle shapes in Chang'e-5 lunar soil. The aspect ratio distribution is fitted with a Gaussian model, showing that it conforms to a normal distribution with a minimum, maximum, mean, median, and mode of 0.04, 1.00, 0.55, 0.56, and 0.59, respectively, which indicates that most of the Chang'e-5 lunar soil particles are between flat and spherical in shape. The cumulative volume distribution of the aspect ratio shows that the 50th percentile is at 0.51. This moderate aspect ratio suggests that most particles are elliptical or slightly flattened in shape. Figure 7d shows the distribution of aspect ratios after classifying particles by size based on the ESD, with average aspect ratios of 0.63, 0.50, 0.50, 0.48, 0.48, 0.48, 0.45, 0.55, and 0.57 for clay, very fine silt, fine silt, medium silt, coarse silt, very fine sand, fine sand, medium sand, and coarse sand types of lunar soil particles, respectively, with no significant fluctuations, proving that particle size has no significant impact on aspect ratio. Gorz et al. 1972 previously analyzed the 2D aspect ratios of fine Apollo lunar soil samples images (<30 μm for Apollo 14 and 15 soils; <6 μm for an Apollo 12 soil) using SEM images. Aspect ratio values ranged from 1.0 to less than 0.1, with the majority between 0.4 and 0.7. Similar to the findings of this study, this demonstrates that the elongation of the fine particles in the lunar soil is similar to that of the Apollo lunar soil.

Sphericity measures how closely the 3D shape of a particle resembles a sphere. Figure 7e showcases selected 3D models of Chang'e-5 lunar soil particles with varying sphericity values. It is evident that the particles with the highest sphericity have axes of similar length between the longest and the shortest and relatively smooth surfaces. Conversely, particles with lower sphericity have a greater disparity between their longest and shortest axes, and their surfaces are rougher. Compared to aspect ratio, sphericity not only considers how close the particle's axes are to each other but also reflects to some extent whether the particle's edges are pronounced. For instance, in Figure 7e, a brown particle with a sphericity of 0.25 has an aspect ratio of 0.73, while an orange particle with a sphericity of 0.40 has an aspect ratio of 0.65. The orange particle is more elongated (lower aspect ratio) than the brown particle, but because its surface edges are comparatively smoother, it results in a higher sphericity. Figure 7f,g presents the spatial and frequency distribution histograms of lunar soil particle sphericity, showing that the minimum, maximum, mean, median, and mode of is 0.13, 1.02, 0.87, 0.89, and 0.93 respectively. The cumulative volume distribution of sphericity shows that the 50th percentile is at 0.88. It can be seen that the sphericity distribution is notably right-skewed, with most lunar soil particles having sphericity values between 0.85 and 1. Particles with low sphericity values are typically polygonal, flat, or elongated. The formation of fine lunar soil primarily relies on space weathering processes such as micrometeorite impacts on the lunar surface (Su et al., 2022), where particles with low sphericity often break and fracture upon impact, and the newly formed particles have increased sphericity as the lunar soil matures and stabilizes. This is the reason for the right-skewed distribution of sphericity values in fine lunar soil. Figure 7h shows the distribution of sphericity for particles classified by size based on the average ESD, with average sphericity values of 0.91, 0.90, 0.83, 0.70, 0.57, 0.44, 0.31, 0.31, 0.13 for clay, very fine silt, fine silt, medium silt, coarse silt, very fine sand, fine sand, medium sand, and coarse sand types of lunar soil particles, respectively. As particle size decreases, the sphericity value significantly increases, confirming the correlation between sphericity and the maturity of lunar soil. On the other hand, the abundant existence of small glass beads (Z. Chen, 2023; Yan et al., 2024; W. Yang et al., 2022; Zhao et al., 2023) in the lunar soil is also the reason for the high average sphericity of fine granular lunar soil. Many glass beads smaller than 10 μm are present in the lunar soil because they melt at the high temperatures created by meteorite impacts and quickly cool and solidify into spheres due to surface tension in the low temperatures of space.

### 5.3 | Overall surface roughness of Chang'e-5 lunar soil

The TRP quantitatively measures the overall surface roughness of 3D objects, defined as the difference between the maximum and minimum radii from the centroid to the boundary points of the object's projection across various planes (XY, YZ, XZ). The TRP value calculation example of one lunar soil particle is shown in Figure 8a. This metric captures the extent of surface irregularities and deviations from an idealized shape. The maximum radius represents the farthest point on the surface from the centroid, indicating the most prominent protrusion, while the minimum radius represents the closest point, indicating the deepest indentation. By calculating the difference between these two values, TRP encapsulates the overall roughness of the surface, integrating the effects of peaks and valleys in the three orthogonal directions on the object's surface.

Figure 8b–d illustrates the spatial distribution of TRP, ESD, frequency distribution statistics, and correlation analysis of the lunar soil samples. The TRP values range from 0.00 to 425.24 μm, with an average value of 3.42 μm. Notably, 95% of the particles have TRP values within the range of 0–10.00 μm, indicating a pronounced skew toward lower values. Furthermore, a linear positive correlation is observed between TRP values and equivalent sphere diameter, with a correlation coefficient of 0.85. This correlation suggests that as particle volume increases, the TRP value also increases, indicating that larger particles possess rougher surfaces and exhibit more significant deviations and irregularities.

A correlation analysis was conducted on the aforementioned 3D morphological parameters of the lunar soil particles. Figure 9 shows the Pearson correlation coefficient matrix of mean Feret diameter, aspect ratio, sphericity, surface area, TRP, and ESD for 553,578 lunar soil particles. It can be observed that, aside from the very strong positive correlation between TRP and ESD (correlation coefficient of 0.92), the other parameters exhibit relatively weak correlations. This finding demonstrates that the measurement parameters selected in this study effectively capture different aspects of the morphological characteristics of the lunar soil.

## 6 | CLUSTER ANALYSIS OF LUNAR SOIL PARTICLES

A clustering analysis was conducted on 553,578 lunar soil particles using six 3D morphological characteristics. Using the K-means algorithm, a clustering analysis was performed on the mean Feret diameter, aspect ratio, sphericity, surface area, ESD, and TRP of all segmented Chang'e-5 lunar soil particles, with the number of clusters set to 30. The clustering effectiveness was evaluated by calculating the Calinski–Harabasz index, and principal component analysis was applied to reduce the data to two dimensions for visualization (Figure 10). The final Calinski–Harabasz index obtained is 34,836,477.73, with the sizes of the 30 clusters being 556,606; 1; 4; 1; 2; 109; 939; 18; 29; 5,946; 1; 224; 3; 21; 108,869; 2; 1,669; 71; 356; 3; 12; 29; 3; 13,100; 123; 5; 554; 39; 2,964; 32,768, indicating that the clustering results are of very high quality. Considering the number and size of the clusters, although the cluster sizes vary greatly, overall, these clusters are able to separate the data points effectively. From each of these

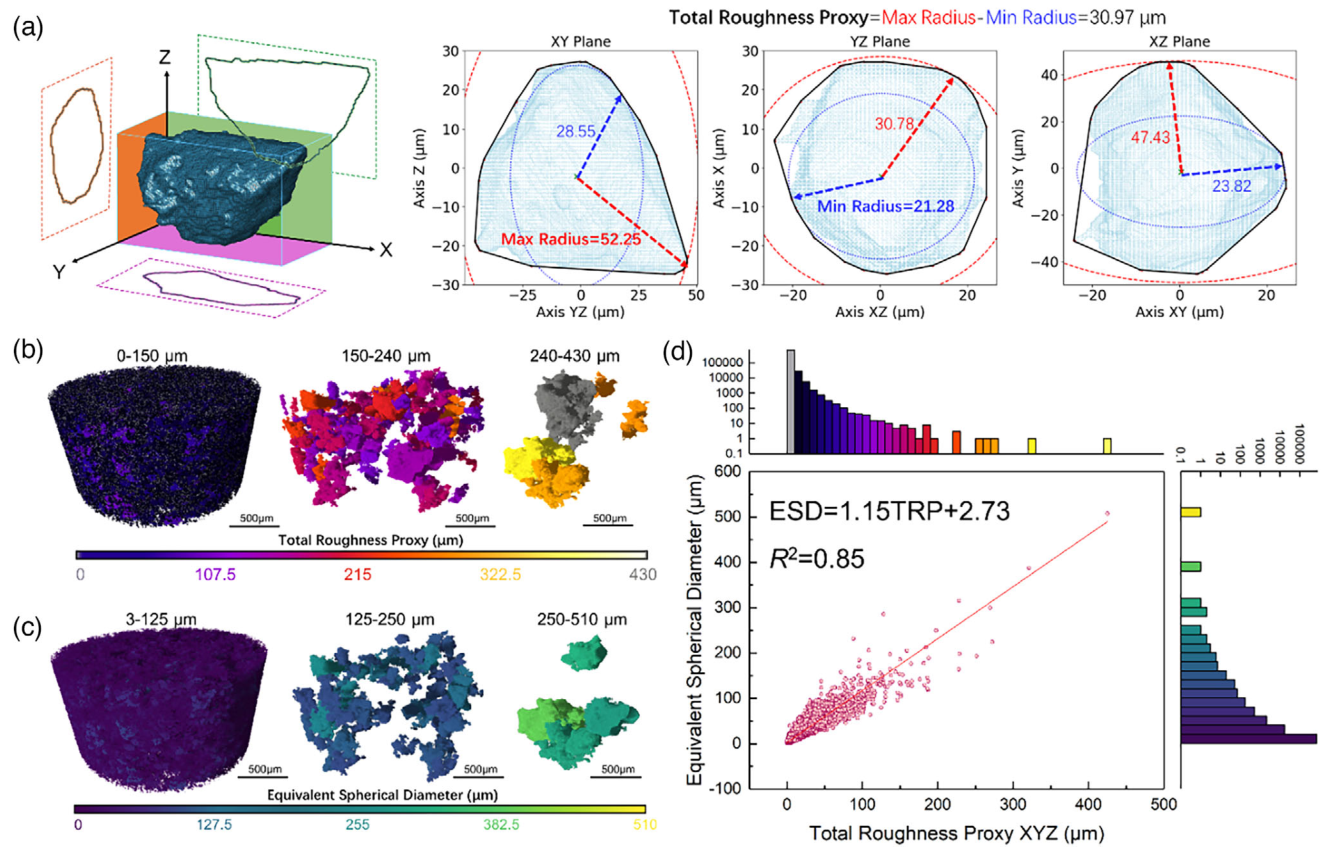


**FIGURE 8** Total roughness proxy (TRP) of Chang'e-5 lunar soil. (a) TRP calculation: differences between max and min centroid distances to projection contours in three orthogonal planes, (b) spatial distribution of particles with varying TRP values, (c) spatial distribution of particles by ESD, and (d) frequency distribution and correlation analysis of TRP and ESD.

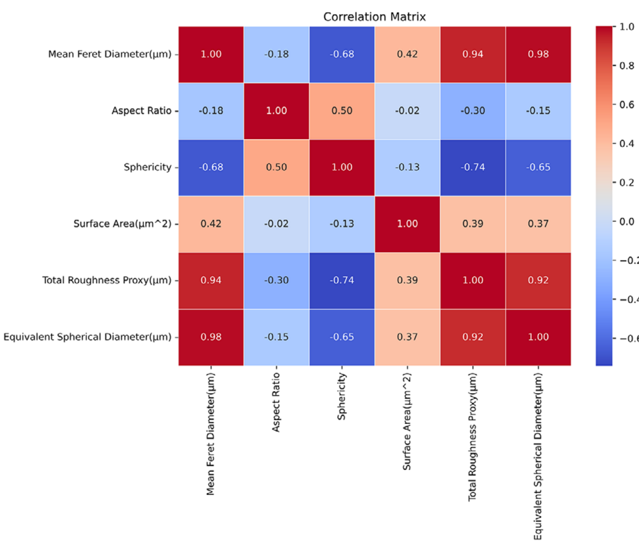


**FIGURE 9** Correlation Analysis of 3D morphological metrics.

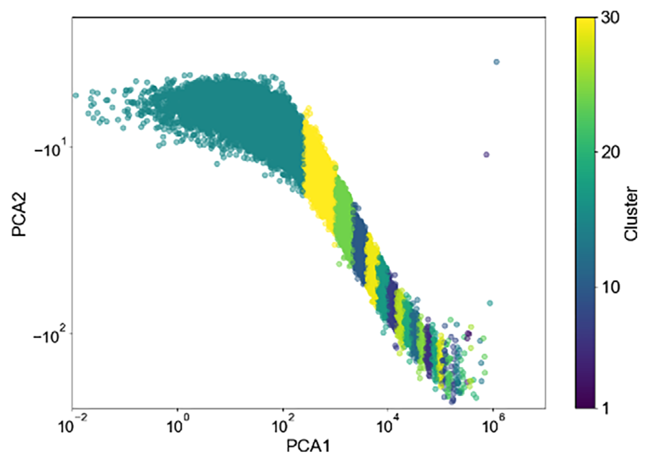


**FIGURE 10** Principal component analysis results based on morphological parameters of Chang'e-5 lunar soil.

30 clusters, one particle was randomly selected as shown in Figure 11. To construct the STL models, the marching cubes algorithm was applied to extract the isosurface from the segmented CT data, generating high-resolution triangular mesh representations of the lunar soil particles. The resulting STL files were further refined through mesh simplification and smoothing to enhance numerical stability for discrete element simulations and engineering applications.

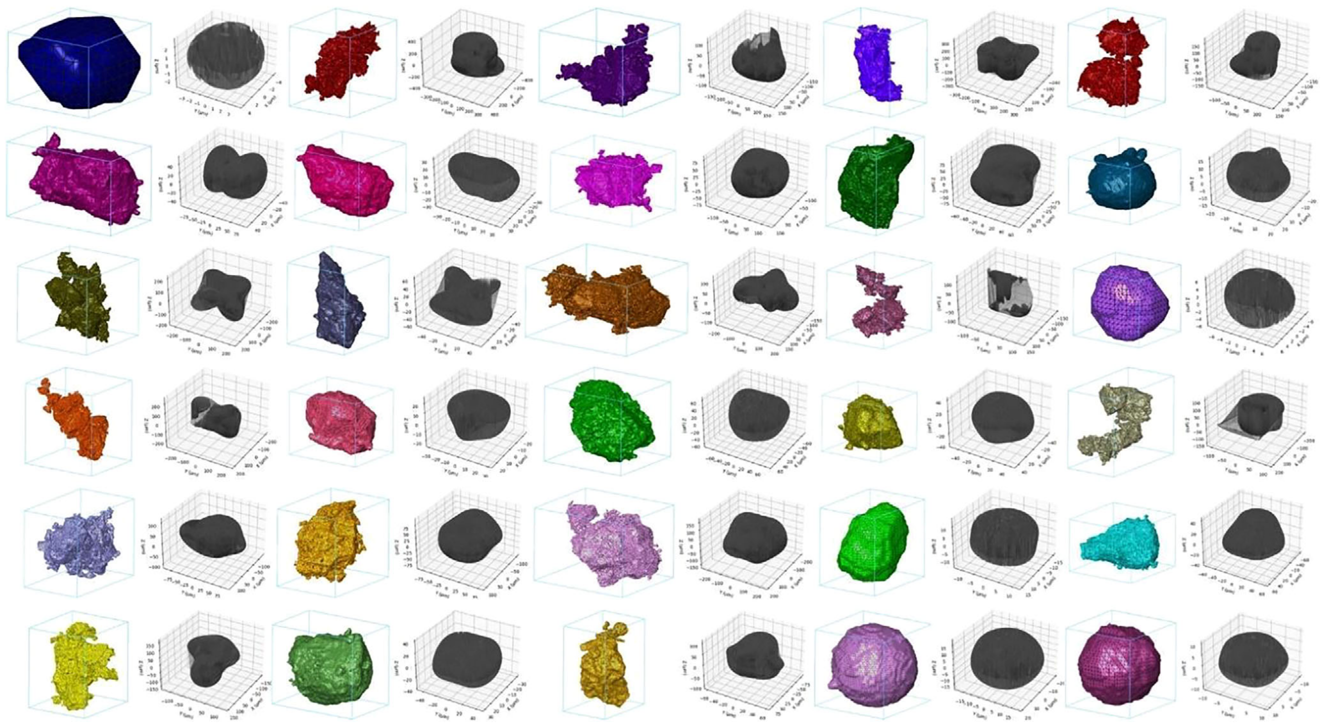

**FIGURE 11** Representative STereoLithography files of lunar soil particles and computed spherical harmonic base surfaces for 3D morphology analysis.

Using the method described in the reference (Michikami et al., 2018), the longest, intermediate, and shortest edges ($L \geq I \geq S$) of the minimum bounding box were calculated and compared with the data of lunar samples returned by the Apollo and Luna (Tsuchiyama et al., 2022) as shown in Figure 12a. If $I/L > 2/3$ and $S/I > 2/3$, the particle is nearly equiaxed and classified as Equant. If $I/L < 2/3$ and $S/I > 2/3$, the particle has two significantly larger dimensions, fitting the Tabular description. If $I/L > 2/3$ and $S/I < 2/3$, the particle has one dimension significantly longer than the others, described as Prismatic. If $I/L < 2/3$ and $S/I < 2/3$, the particle's length is much greater than its width and height, resembling a needle-like shape, fitting the description of Acicular. It is observed that the Chang'e-5 lunar soil particles, similar to previously returned lunar samples, are predominantly of the Equant type, with only a few particles classified as Acicular and Tabular.

Subsequently, the 3D local roughness of 30 representative particles selected from the resulting clusters was calculated. Local 3D roughness refers to the small-scale irregularities with minor peaks and valleys on the particle surface. Determining the reference surface is crucial for measuring the local roughness of 3D irregular particles. In this study, the spherical harmonic reconstruction method was used to obtain the reference surface of the particles, retaining the overall morphological characteristics while removing particle textures to obtain a smooth surface as the reference. First, the marching cubes algorithm was used to extract the 3D volumetric data of the 30 particles and save them as STL files. This algorithm traverses the voxel data, generates corresponding isosurface triangular meshes, and optimizes them through simplification, smoothing, and removal of isolated components to create STL files. Then, the vertices and faces of the 3D mesh models from the STL files were extracted. After converting the vertex coordinates to spherical coordinates, a 5th-order spherical harmonic function was used to fit the vertex coordinates and reconstruct a smooth reference surface (Figure 11). The local roughness was obtained by calculating the distance between each vertex and the reference surface. Next, the total area of the reference surface was then calculated, and local roughness was integrated to derive the 3D arithmetic average roughness ($S_a$). Finally, the local roughness was normalized and rainbow and reference surface plots were generated to visualize the roughness distribution and shape of the mesh models as shown in Figure 12c.

Unlike TRP, local roughness can reflect the small-scale surface undulations that directly affect particle interactions such as collision, friction, and embedding. Figure 12b shows the average local roughness ($S_a$) of the selected 30 particles, with an average value of 15.8 μm, a maximum value of 64.7 μm (Particle No. 2), and a minimum value of 0.23 μm (Particle No. 1). Unlike TRP, local roughness can reflect the small-scale surface undulations

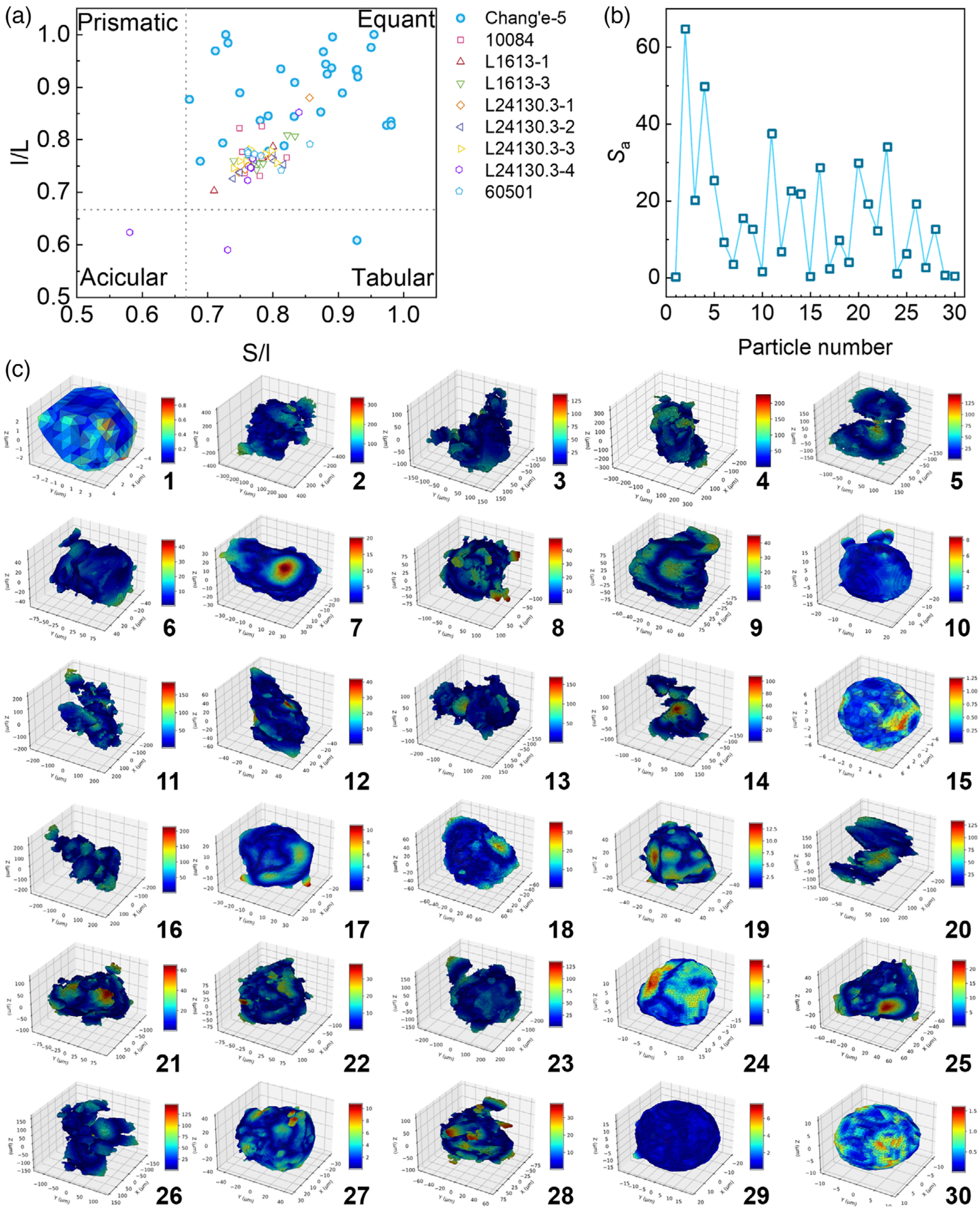


**FIGURE 12** Local 3D surface roughness of selected Chang'e-5 lunar soil particles. (a) Zingg diagrams of lunar regolith particles displaying typical shape distributions. $L$, $I$, and $S$ represent the longest, intermediate, and shortest edge lengths of the particle's minimum bounding box ($L \geq I \geq S$), respectively. Chang'e-5 represents 30 representative lunar soil particles extracted through cluster analysis in this study. 10084 represents lunar samples from Mare Tranquillitatis collected by the US Apollo 11 mission. L1613-1 and L1613-3 represent lunar samples from Mare Fecunditatis collected by the Soviet Luna 16 mission. The samples starting with L24 represent lunar samples from Mare Crisium collected by Luna 24 mission. 60501 represents lunar samples from the Descartes Highlands collected by the US Apollo 16 mission (Tsuchiyama et al., 2022). (b) The average of local roughness ($S_a$) of 30 selected Chang'e-5 samples. (c) The calculation results of the local roughness of 30 selected Chang'e-5 lunar soil particles.

that directly affect particle interactions such as collision, friction, and embedding. The STL files for the 30 particles are available on request of the authors, which can be used to construct numerical models of lunar soil particles.

## 7 | POTENTIAL UTILIZATION OF 3D MORPHOLOGICAL CHARACTERISTICS OF LUNAR SOIL IN DISCRETE ELEMENT SIMULATION

DEM is a numerical computation method used to simulate the dynamic behavior of particle systems (Espinosa et al., 2023). The main steps include particle model creation, initial sample preparation, contact model definition, particle property definition, boundary condition setting, and dynamic equation solving. This process ultimately provides the motion trajectories and mechanical responses of lunar soil and other particulate materials under external loads.

The 3D morphology parameters of Chang'e-5 lunar soil can be applied to the modeling steps of DEM simulations to enhance accuracy. Specifically, for particle model creation, size parameters such as ESD can be used to describe particle size, forming the basis for simplified particle models. Moreover, open-source STL models can be directly imported into common commercial software to establish precise geometric models of particles. For initial sample preparation, the centroid position of individual particles can determine their initial positions within the simulation domain. Combined with the layered underpressure method, this can create high-fidelity initial samples, improving simulation accuracy. The centroid position also plays a crucial role in calculating dynamic parameters such as the particles' moments of inertia. Regarding contact model definition, DEM typically employs linear elastic contact models or Hertz contact models to describe contact issues between smooth particles. However, these models are not suitable for rough surfaces. Local roughness describes the microstructure of particle surfaces within contact models, affecting inter-particle friction, contact stiffness, and contact area. By incorporating local roughness into contact models, more accurate physical phenomena can be reflected. Additionally, most lunar soil particles have irregular shapes, with face-to-face contact being most common, exhibiting a certain resistance to rotation known as the interlocking effect. Through 3D morphology parameters such as sphericity and aspect ratio, the torsional resistance coefficient can be quantitatively predicted (Rorato et al., 2021), thus improving the contact model.

## 8 | CONCLUSION

In this study, we applied high-resolution X-ray CT and deep learning techniques to analyze the 3D morphological characteristics of lunar soil particles from the Chang'e-5 mission. Using a U-Net deep learning network, we developed a non-destructive, automated method to characterize 553,578 particles, extracting key parameters such as size, shape, and surface roughness. The results indicate that 74.3% of particles are smaller than 100 μm, with a median ESD of 63.73 μm. The particles are predominantly elliptical or slightly flattened, with finer particles exhibiting higher sphericity (average 0.87). Surface roughness analysis revealed that larger particles tend to have more irregular surfaces, influencing mechanical interactions. The clustering analysis classified particles into 30 representative types, providing insights into particle morphology variations and microstructural characteristics. These findings enhance the understanding of lunar soil's mechanical behavior, which is critical for DEM simulations and in situ resource utilization applications such as sintering-based construction. This research lays the groundwork for sustainable lunar infrastructure, including landing pads, rover mobility optimization, and lunar base construction. Additionally, the proposed method can be extended to other planetary regolith studies, offering a scalable and efficient approach for extraterrestrial soil analysis.

## ACKNOWLEDGMENTS

The author expresses their thanks to the China National Space Administration for providing the invaluable Chang'e-5 sample (No. CE5C0400YJFM00406). This work was supported by the National Natural Science Foundation of China (52308427), the Fundamental Research Funds for the Central Universities, China Postdoctoral Science Foundation (2024T171118), and B-type Strategic Priority Program of the Chinese Academy of Sciences (XDB41000000).

## REFERENCES

Alam, K. M. R., Siddique, N., & Adeli, H. (2020). A dynamic ensemble learning algorithm for neural networks. *Neural Computing and Applications*, *32*(12), 8675–8690.

Bao, C., Zhang, D., Wang, Q., Cui, Y., & Feng, P. (2024). Lunar in situ large-scale construction: Quantitative evaluation of regolith solidification techniques. *Engineering*, *39*, 204–221.

Cao, K., Dong, M., She, Z., Xiao, Q., Wang, X., Qian, Y., Li, Y., Wang, Z., He, Q., Wu, X., Zong, K., Hu, Z., & Xiao, L. (2022). A novel method for simultaneous analysis of particle size and mineralogy for Chang'e-5 lunar soil with minimum sample consumption. *Science China Earth Sciences*, *65*(9), 1704–1714.

Carrier, W. D., III, Olhoeft, G. R., & Mendell, W. (1991). Physical properties of the lunar surface. In G. H. Heiken, D. T. Vaniman, & B.

M. French (Eds.), *Lunar sourcebook, a user's guide to the moon*. Cambridge University Press (pp. 305–307).

Chen, D., Li, Y., Tao, J., Li, Y., Zhang, S., Shan, X., Wang, T., Qiao, Z., Zhao, R., Fan, X., & Zhou, Z. (2024). Deep learning-based segmentation model for permeable concrete meso-structures. *Computer-Aided Civil and Infrastructure Engineering*, *39*(23), 3626–3645.

Chen, Y., Hu, S., Li, J., Li, Q., Li, X., Li, Y., Liu, Y., Qian, Y., Yang, W., Zhou, Q., Lin, Y., Li, C., & Li, X. (2023). Chang'e-5 lunar samples shed new light on the moon. *The Innovation Geoscience*, *1*(1), 100014.

Chen, Z., Zhao, Y., Chi, X., Yan, Y., Shen, J., Zou, M., Zhao, S., Liu, M., Yao, W., Zhang, B., Ke, H., Ma, X.-L., Bai, H., Yang, M., Zou, Z., & Wang, W.-H. (2023). Geological timescales' aging effects of lunar glasses. *Science Advances*, *9*(45), eadi6086.

Chien, S. A., Visentin, G., & Basich, C. (2024). Exploring beyond Earth using space robotics. *Science Robotics*, *9*(91), eadi6424.

De Nardin, A., Zottin, S., Piciarelli, C., Colombi, E., & Foresti, G. L. (2023). Few-shot pixel-precise document layout segmentation via dynamic instance generation and local thresholding. *International Journal of Neural Systems*, *33*(10), 2350052.

Ding, L., Zhou, R., Yu, T., Yang, H., He, X., Gao, H., Wang, J., Yuan, Y., Wang, J., Wang, Z., Qi, H., Li, J., Feng, W., Li, X., Liu, C., Han, S., Zeng, X., Zhao, Y.-Y. S., Liu, G., … Zhang, K. (2024). Lunar rock investigation and tri-aspect characterization of lunar farside regolith by a digital twin. *Nature Communications*, *15*(1), 2098.

Ding, L., Zhou, R., Yuan, Y., Yang, H., Li, J., Yu, T., Liu, C., Wang, J., Li, S., Gao, H., Deng, Z., Li, N., Wang, Z., Gong, Z., Liu, G., Xie, J., Wang, S., Rong, Z., Deng, D., … Di, K. (2022). A 2-year locomotive exploration and scientific investigation of the lunar farside by the Yutu-2 rover. *Science Robotics*, *7*(62), eabj6660.

Espinosa, M., Martínez-Ortíz, L., Alonso-Llanes, L., Rodríguez-de-Torner, L. A., Chávez-Linares, O., & Altshuler, E. (2023). Imperfect bodies sink imperfectly when settling in granular matter. *Science Advances*, *9*(19), eadf6243.

Falk, T., Mai, D., Bensch, R., Çiçek, Ö., Abdulkadir, A., Marrakchi, Y., Böhm, A., Deubner, J., Jäckel, Z., Seiwald, K., Dovzhenko, A., Tietz, O., Dal Bosco, C., Walsh, S., Saltukoglu, D., Tay, T. L., Prinz, M., Palme, K., Simons, M., … Ronneberger, O. (2019). U-Net: Deep learning for cell counting, detection, and morphometry. *Nature Methods*, *16*(1), 67–70.

García-Aguilar, I., García-González, J., Luque-Baena, R. M., López-Rubio, E., & Domínguez, E. (2023). Optimized instance segmentation by super-resolution and maximal clique generation. *Integrated Computer-Aided Engineering*, *30*(3), 243–256.

Gorz, H., White, E. W., Johnson, G. G., Jr., & Pearson, M. W. (1972). Cesemi studies of Apollo 14 and 15 fines. *Lunar and Planetary Science Conference Proceedings*, *3*, 3195.

Graf, J. C. (1993). *Lunar soils grain size catalog*. National Aeronautics and Space Administration.

Gupta, N., Dawara, V., Kumar, A., & Viswanathan, K. (2024). Liquid state sintering enhances consolidation in basalt-rich lunar regolith. *Advances in Space Research*, *74*(4), 1693–1705.

Hu, S., He, H., Ji, J., Lin, Y., Hui, H., Anand, M., Tartèse, R., Yan, Y., Hao, J., Li, R., Gu, L., Guo, Q., He, H., & Ouyang, Z. (2021). A dry lunar mantle reservoir for young mare basalts of Chang'e-5. *Nature*, *600*(7887), 49–53.

Ikotun, A. M., Ezugwu, A. E., Abualigah, L., Abuhaija, B., & Heming, J. (2023). K-means clustering algorithms: A comprehensive review, variants analysis, and advances in the era of big data. *Information Sciences*, *622*, 178–210.

Jiang, M., Shen, Z., & Thornton, C. (2013). Microscopic contact model of lunar regolith for high efficiency discrete element analyses. *Computers and Geotechnics*, *54*, 104–116.

Jiang, Y., Li, Y., Liao, S., Yin, Z., & Hsu, W. (2022). Mineral chemistry and 3D tomography of a Chang'e 5 high-Ti basalt: Implication for the lunar thermal evolution history. *Science Bulletin*, *67*(7), 755–761.

Katagiri, J., Matsushima, T., Yamada, Y., Tsuchiyama, A., Nakano, T., Uesugi, K., Ohtake, M., & Saiki, K. (2015). Investigation of 3D grain shape characteristics of lunar soil retrieved in Apollo 16 using image-based discrete-element modeling. *Journal of Aerospace Engineering*, *28*(4), 04014092.

Li, C., Hu, H., Yang, M.-F., Pei, Z.-Y., Zhou, Q., Ren, X., Liu, B., Liu, D., Zeng, X., Zhang, G., Zhang, H., Liu, J., Wang, Q., Deng, X., Xiao, C., Yao, Y., Xue, D., Zuo, W., Su, Y., … Ouyang, Z. (2022). Characteristics of the lunar samples returned by the Chang'e-5 mission. *National Science Review*, *9*(2), nwab188.

Li, C., Wang, C., Wei, Y., & Lin, Y. (2019). China's present and future lunar exploration program. *Science*, *365*(6450), 238–239.

Liu, X., Gu, L., Tian, H.-C., Li, J., Tang, X., Hu, S., & Lin, Y. (2024). First classification of iron meteorite fragment preserved in Chang'e-5 lunar soils. *Science Bulletin*, *69*(4), 554–561.

Lu, X., Bertei, A., Finegan, D. P., Tan, C., Daemi, S. R., Weaving, J. S., O'Regan, K. B., Heenan, T. M. M., Hinds, G., Kendrick, E., Brett, D. J. L., & Shearing, P. R. (2020). 3D microstructure design of lithium-ion battery electrodes assisted by X-ray nano-computed tomography and modelling. *Nature Communications*, *11*(1), 2079.

Mandt, K. E. (2024). The scientific importance of the lunar environment. *Science*, *384*(6692), eado9563.

McKay, D., Fruland, R., & Heiken, G. (1974). Grain size and the evolution of lunar soil. *Lunar Science Conference*, Houston, TX (pp. 887–906).

Metzger, P. T., Smith, J., & Lane, J. E. (2011). Phenomenology of soil erosion due to rocket exhaust on the moon and the Mauna Kea lunar test site. *Journal of Geophysical Research: Planets*, *116*(E6), E06005.

Michikami, T., Kadokawa, T., Tsuchiyama, A., Hagermann, A., Nakano, T., Uesugi, K., & Hasegawa, S. (2018). Influence of petrographic textures on the shapes of impact experiment fine fragments measuring several tens of microns: Comparison with Itokawa regolith particles. *Icarus*, *302*, 109–125.

Mitra, S., Paris, R., Bernard, L., Abbal, R., Charrier, P., Falvard, S., Costa, P., & Andrade, C. (2024). X-ray tomography applied to Tsunami deposits: Optimized image processing and quantitative analysis of particle size, particle shape, and sedimentary fabric in 3D. *Marine Geology*, *470*, 107247.

Olhoeft, G. R., Frisillo, A. L., & Strangway, D. W. (1974). Electrical properties of lunar soil sample 15301,38. *Journal of Geophysical Research*, *79*(11), 1599–1604.

Pereira, D. R., Piteri, M. A., Souza, A. N., Papa, J. P., & Adeli, H. (2020). FEMa: A finite element machine for fast learning. *Neural Computing and Applications*, *32*, 6393–6404.

Rafiei, M. H., Gauthier, L. V., Adeli, H., & Takabi, D. (2022). Self-supervised learning for electroencephalography. *IEEE Transactions on Neural Networks and Learning Systems*, *35*(2), 1457–1471.

Rafiei, M. H., Khushefati, W. H., Demirboga, R., & Adeli, H. (2017). Supervised deep restricted Boltzmann machine for estimation of concrete. *ACI Materials Journal*, *114*(2), 237.

Ronneberger, O., Fischer, P., & Brox, T. (2015). U-Net: Convolutional networks for biomedical image segmentation. In N. Navab, J. Hornegger, W. M. Wells, & A. F. Frangi (Eds.), *Lecture notes in computer science*: Vol. *9351*. Medical image computing and computer-assisted intervention—MICCAI 2015 (pp. 234–241). Springer International Publishing.

Rorato, R., Arroyo, M., Gens, A., Andò, E., & Viggiani, G. (2021). Image-based calibration of rolling resistance in discrete element models of sand. *Computers and Geotechnics*, *131*, 103929.

Sarwar, S. A., & Hasnain, Z. (2024). Investigating collision effects on lunar soil particles ejected under rocket plumes. *Acta Astronautica*, *218*, 114–125.

Schörghofer, N., & Rufu, R. (2023). Past extent of lunar permanently shadowed areas. *Science Advances*, *9*(37), eadh4302.

Su, B., Yuan, J., Chen, Y., Yang, W., Mitchell, R. N., Hui, H., Wang, H., Tian, H., Li, X.-H., & Wu, F.-Y. (2022). Fusible mantle cumulates trigger young mare volcanism on the cooling moon. *Science Advances*, *8*(42), eabn2103.

Sun, S., Wang, P., Peng, H., & Liu, Z. (2024). Referring image segmentation with multi-modal feature interaction and alignment based on convolutional nonlinear spiking neural membrane systems. *International Journal of Neural Systems*, *34*(12), 2450064.

Tsuchiyama, A., Sakurama, T., Nakano, T., Uesugi, K., Ohtake, M., Matsushima, T., Terakado, K., & Galimov, E. M. (2022). Three-dimensional shape distribution of lunar regolith particles collected by the Apollo and Luna programs. *Earth, Planets and Space*, *74*(1), 172.

Udden, J. A. (1914). Mechanical composition of clastic sediments. *GSA Bulletin*, *25*(1), 655–744.

Vincent, L., & Soille, P. (1991). Watersheds in digital spaces: An efficient algorithm based on immersion simulations. *IEEE Transactions on Pattern Analysis and Machine Intelligence*, *13*(6), 583–598.

Wang, J., Zhang, L., & Zhang, Y. (2023). Mixture 2D convolutions for 3D medical image segmentation. *International Journal of Neural Systems*, *33*(1), 2250059.

Wang, S., & Jiang, M. (2024). Lunar regolith simulations with discrete element method based on Chang'e-5 mission's lunar soil particle morphology. *Chinese Journal of Geotechnical Engineering*, *46*(4), 833–842.

Wang, Y., Hao, L., Li, Y., Sun, Q., Sun, M., Huang, Y., Li, Z., Tang, D., Wang, Y., & Xiao, L. (2022). In-situ utilization of regolith resource and future exploration of additive manufacturing for lunar/martian habitats: A review. *Applied Clay Science*, *229*, 106673.

Wentworth, C. K. (1922). A scale of grade and class terms for clastic sediments. *The Journal of Geology*, *30*(5), 377–392.

Wu, Y., Liao, S., Yan, P., Xiao, Z., Yin, Z., Yang, W., Wang, H., Tian, H., Hui, H., Pan, L., Ma, H., Wu, S., & Hsu, W. (2023). Impact-related chemical modifications of the Chang'e-5 lunar regolith. *Geochimica et Cosmochimica Acta*, *363*, 94–113.

Yan, P., Xiao, Z., Wu, Y., Wu, Y., Pan, Q., Luo, F., & Xu, R. (2024). Submicroscopic iron-rich grains throughout impact glasses in Chang'e-5 regolith. *Icarus*, *410*, 115920.

Yang, L., Cai, B., Zhang, R., Li, K., Zhang, Z., Lei, J., Chen, B., & Wang, R. (2020). Mechanical analysis and performance optimization for the lunar rover's vane-telescopic walking wheel. *Engineering*, *6*(8), 936–943.

Yang, W., Chen, Y., Wang, H., Tian, H.-C., Hui, H., Xiao, Z., Wu, S.-T., Zhang, D., Zhou, Q., Ma, H.-X., Zhang, C., Hu, S., Li, Q.-L., Lin, Y., Li, X.-H., & Wu, F.-Y. (2022). Geochemistry of impact glasses in the Chang'e-5 regolith: Constraints on impact melting and the petrogenesis of local basalt. *Geochimica et Cosmochimica Acta*, *335*, 183–196.

Yao, Y., Wang, L., Zhu, X., Tu, W., Zhou, Y., Liu, R., Sun, J., Tao, B., Wang, C., Yu, X., Gao, L., Cao, Y., Wang, B., Li, Z., Yao, W., Xiong, Y., Yang, M., Wang, W., & Zou, Z. (2022). Extraterrestrial photosynthesis by Chang'e-5 lunar soil. *Joule*, *6*(5), 1008–1014.

Yu, C., Wu, W., Zheng, J., Zeng, W., Zheng, D., Li, Z., Chen, C., & Wang, S. (2025). A multi-stage adaptive otsu thresholding algorithm for pore segmentation in rock thin-section images. *Earth Science Informatics*, *18*, 239.

Zeng, X., Wu, Y., Yu, W., Mo, B., Wen, Y., Zhao, X., Li, X., Zhang, X., & Liu, J. (2024). Unusual Ti minerals on the moon produced by space weathering. *Nature Astronomy*, *8*(6), 732–738.

Zhang, H., Zhang, X., Zhang, G., Dong, K., Deng, X., Gao, X., Yang, Y., Xiao, Y., Bai, X., Liang, K., Liu, Y., Ma, W., Zhao, S., Zhang, C., Zhang, X., Song, J., Yao, W., Chen, H., Wang, W., … Yang, M. (2021). Size, morphology, and composition of lunar samples returned by Chang'e-5 mission. *Science China Physics, Mechanics & Astronomy*, *65*(2), 229511.

Zhang, R., Zhou, S., & Li, F. (2022). Preparation of geopolymer based on lunar regolith simulant at in-situ lunar temperature and its durability under lunar high and cryogenic temperature. *Construction and Building Materials*, *318*, 126033.

Zhao, R., Shen, L., Xiao, D., Chang, C., Huang, Y., Yu, J., Zhang, H., Liu, M., Zhao, S., Yao, W., Lu, Z., Sun, B., Bai, H., Zou, Z., Yang, M., & Wang, W. (2023). Diverse glasses revealed from Chang'e-5 lunar regolith. *National Science Review*, *10*(12), nwad079.

Zhou, C., Mo, B., Tang, H., Gu, Y., Li, X., Zhu, D., Yu, W., & Liu, J. (2024). Multiple sources of water preserved in impact glasses from Chang'e-5 lunar soil. *Science*, *10*(19), eadl2413.

Zhou, S., Lu, C., Zhu, X., & Li, F. (2021). Preparation and characterization of high-strength geopolymer based on Bh-1 lunar soil simulant with low alkali content. *Engineering*, *7*(11), 1631–1645.

**How to cite this article:** Zhou, S., Jiang, Y., Tao, X., Li, F., Zhang, C., Yang, W., & Gao, Y. (2025). Three-dimensional morphological analysis of Chang'e-5 lunar soil using deep learning-automated segmentation on computed tomography scans. *Computer-Aided Civil and Infrastructure Engineering*, *40*, 5076–5092. https://doi.org/10.1111/mice.13487